Environmental Research 251 (2024) 118672

Contents lists available at ScienceDirect

Environmental Research

journal homepage: www.elsevier.com/locate/envres

Improved photocatalytic performance of TiO_2/carbon photocatalysts: Role of carbon additive

C. Abreu-Jaureguí [a], L. Andronic [b], A. Sepúlveda-Escribano [a], J. Silvestre-Albero [a,*]

[a] Laboratorio de Materiales Avanzados, Departamento de Química Inorgánica – Instituto Universitario de Materiales, Universidad de Alicante, Spain
[b] Product Design, Mechatronics and Environment Department, Transilvania University of Brasov, Romania

ARTICLE INFO

Keywords:
Photocatalysis
Oxide/carbon
Interfacial phenomena
Rhodamine B

ABSTRACT

A series of TiO_2 – based photocatalysts have been prepared by the incorporation of 10 wt% of various carbon-based nanomaterials as modifying agents to titania. More specifically, commercial TiO_2 P25 was modified through a wet impregnation approach with methanol with four different carbon nanostructures: single-walled carbon nanotubes (SWCNTs), partially reduced graphene oxide (prGO), graphite (GI), and graphitic carbon nitride (gCN). Characterization results (XPS and Raman) anticipate the occurrence of important interfacial phenomena, preferentially for samples TiO_2/SWCNT and TiO_2/prGO, with a binding energy displacement in the Ti 2p contribution of 1.35 eV and 1.54 eV, respectively. These findings could be associated with an improved electron-hole mobility at the carbon/oxide interface. Importantly, these two samples constitute the most promising photocatalysts for Rhodamine B (RhB) photodegradation, with nearly 100% conversion in less than 2 h. These promising results must be associated with intrinsic physicochemical changes at the formed heterojunction structure and the potential dual-role of the composites able to adsorb and degrade RhB simultaneously. Cyclability tests confirm the improved performance of the composites (e.g., TiO_2/SWCNT, 100% degradation in 1 h) due to the combined adsorption/degradation ability, although the regeneration after several cycles is not complete due to partial blocking of the inner cavities in the carbon nanotubes by non-reacted RhB. Under these reaction conditions, Rhodamine-B xanthene dye degrades via the de-ethylation route.

1. Introduction

Advanced oxidation processes driven by natural sunlight are the key to the next generation wastewater treatment technologies (Ameta et al., 2018). Photocatalysis using semiconductor materials constitutes a promising approach to degrade organic contaminants in wastewater with minimal generation of secondary pollutants (Ren et al., 2021). The photocatalytic reaction path emulates the photosynthesis mechanism, characterized by the creation of highly reactive oxidants and radicals (mainly $\cdot OH$ and O_2^-) within the reaction sites (Bukhov et al., 2004). This leads to the breakdown of pollutants in wastewater, triggered by exposure to a light source with energy levels superior or equal to the energy gap between the valence and the conduction band of the semiconductor. Several materials have emerged due to their outstanding photocatalytic activity; however, titanium dioxide (TiO_2) is the most widely applied photocatalyst due to its promising performance in a wide range of processes, preferentially the commercial formulation known as P25. This formulation is characterized by a perfectly defined anatase/rutile ratio and some amorphous TiO_2 (Jiang et al., 2018). Along the positive features of P25, those that stand out are its high chemical purity, strong stability, low toxicity, high oxidation ability due to an efficient charge-carrier separation, and excellent dispersion in liquid media. A limitation associated with TiO_2 P25 is its exclusive reactivity under UV irradiation, coupled with a rapid rate of electron-hole recombination (from picoseconds to nanoseconds, depending on the band bending), which inevitably decreases quantum efficiency (Ozawa et al., 2014). These limitations contradict the photocatalytic principle of harnessing sunlight, which is approximately composed of 42%–43% of visible light, 52–55% near-infrared (NIR) light, and only 4% of UV light (Wang et al., 2017). Different approaches have been reported in the literature to expand the applicable range of TiO_2 as an efficient photocatalyst, generally focusing on structural modifications. Approaches like structural doping (e.g., surface heteroatoms, doped rare metals, etc.) or the design of TiO_2-based composite materials (e.g., using carbon materials) have shown promising results to modulate the photoactivity of TiO_2 towards the visible range, and to minimize electron-charge

---

[*] Corresponding author.
E-mail address: joaquin.silvestre@ua.es (J. Silvestre-Albero).

https://doi.org/10.1016/j.envres.2024.118672
Received 24 November 2023; Received in revised form 26 February 2024; Accepted 9 March 2024
Available online 18 March 2024
0013-9351/© 2024 The Authors. Published by Elsevier Inc. This is an open access article under the CC BY-NC-ND license (http://creativecommons.org/licenses/by-nc-nd/4.0/).

recombination through the creation of structural defects (Doan Nguyen et al., 2022; Ghumro et al., 2022; Kumar et al., 2011; Zhang et al., 2016; Zhao et al., 2022). In the specific case of carbon as modifiers, the development of an extended oxide-carbon interface has been proposed to enhance charge mobility, thereby minimizing fast recombination, with the associated enhancement in the photocatalytic activity. However, the real role of the carbon structure in the photocatalytic process and how the carbon nature can alter/modify the performance of TiO_2 nanoparticles is still unclear. To the best of our knowledge, these studies have been indistinctly focused on individual species. Therefore, a thoughtful comparison among all these materials is not straightforward since it relies on comparable experimental conditions. Furthermore, a common factor for all these carbon species, not always evaluated in the literature, is their adsorption ability, a highly valuable feature in liquid-phase wastewater treatment. Based on these premises, the present study proposes a comparative examination of four different carbon nanostructures – namely, graphitic carbon nitride (gCN), partially reduced graphene oxide (prGO), graphite (GI), and single-walled carbon nanotubes (SWCNTs) – when employed as modifiers for the commercial titanium dioxide P25. To identify the role of the carbon modifier, we targeted Rhodamine B photodegradation as a case study. Even though it is banned by the European Food Safety Authority (EFSA) (EFSA, 2005), this dye is widely used in industry (textile, plastic, wool, paper, leather) for its value as a coloring agent, water tracer, fluorescent marker, among others (Yusuf et al., 2022). This xanthene derivative has high solubility and stable characteristics, making it challenging to undergo degradation. Furthermore, released in water bodies produces severe environmental issues and health risks for humans and animals. More specifically, water effluents with concentrations surpassing 14 mg/L become highly toxic for aquatic and human organisms, a deeply concerning scenario considering the potential neurological toxicity, carcinogenicity, and mutagenicity associated with RhB (Gao et al., 2016; Skjolding et al., 2021). Focusing our efforts on the liquid phase degradation of this critical dye will contribute to 6 out of 17 sustainable development goals proposed by the United Nations as part of the Global Agenda for 2030.

2. Experimental results

2.1. Synthesis of the supports and photocatalysts

For this study, four different carbon materials were selected: (i) SWCNTs, (ii) pr-GO, (iii) graphite, and (iv) g-C_3N_4. These carbon materials were used as additives to modify the physicochemical properties of commercial TiO_2 P25 and further tested in the photodegradation of Rhodamine B.

TiO_2 Aeroxide© was acquired from Evonik Resource Efficiency GmbH (Germany) as a nano-sized powder. Partially reduced graphene oxide (prGO, AV-40-3-20) was acquired from Avanzare Innovacion Tecnologica S.L., Spain. Synthetic graphite (GI, TIMREX SFG-6 BA-080-M) was supplied by IMERYS Graphite and Carbon, Switzerland. Purified single-walled carbon nanotubes (SWCNT-PT-025-X01) were obtained from Nano-C, Inc. USA. All reagents used in this study were of analytic grade and were used without further purification. Rhodamine-B ($C_{28}H_{31}ClN_2O_3$) and Melamine ($C_3H_6N_6$) were purchased from Sigma – Aldrich.

TiO_2/carbon photocatalysts were prepared through a wet impregnation approach. More specifically, a TiO_2 P25:carbon mixture (90:10 wt ratio) was suspended in methanol and mixed in an ultrasonic bath for 30 min. Afterward, the mixture was stirred in a hot bath until complete solvent evaporation and finally dried at 80 °C overnight. The dried samples were grounded before use. As described above, all carbon materials were commercially available and used without further purification, except C_3N_4. Graphitic carbon nitride was synthesized from melamine by a simple calcination process at 540 °C (4h, 3 °C/min) and finally grounded (Suyana et al., 2021).

2.2. Physicochemical characterization of supports and photocatalysts

A wide variety of techniques were applied to get insights into the textural and chemical properties of the synthesized photocatalysts. Textural properties were evaluated using nitrogen adsorption at cryogenic temperatures (−195 °C). Prior to the adsorption measurements, samples were submitted to an outgassing treatment at 250 °C for 8h. Gas adsorption measurements were performed in a home-made manometric equipment designed and constructed by the LMA group. X-ray diffraction patterns (XRD) were used to identify the crystallographic structure of the synthesized composites. These analyses were performed in a Panalytical Empyrean multifunctional equipment equipped with an X-ray tube, Cu Kα cathode, and a PIXcel 3D detector. XPS analyses were performed in a fully automated Thermo-Scientific K-Alpha spectrometer. Raman spectra were collected on a Jasco NRS-5100 dispersive equipment using 532.1 nm as the laser excitation wavelength with a power of 2.1 mW at a resolution of 3.62 cm^{-1}/pixel. Transmission electron microscopy (TEM) images were performed in a JEOL JEM-1400 Plus apparatus with an electron beam of 200 keV. Energy gap and band position were calculated according to the Kubelka-Munk function and Tauc method based on the information obtained from the Diffuse Reflectance (DR) and Ultraviolet Photoelectron Spectroscopy (UPS) analysis. DR was performed in a Jasco V-670 dual-beam UV–Vis/NIR spectrometer covering 200–1000 nm. Meanwhile, UPS was applied using an automated Thermo-Scientific NEXSA multi-surface analyzer with a high resolution near the zero eV zone, where the valence band is located.

2.3. Photocatalytic degradation of Rhodamine B

The degradation of RhB was evaluated in a home-built photoreactor equipped with 24 lamps (18 W/lamp) equally distributed in the circular reactor (i.d., 1 m). Half of the lamps correspond to blacklight blue UV tubes, and the other half corresponds to visible TL-D Food tubes, both from Philips. The tubular reactor has five integrated stirring positions and a cooling system to maintain constant temperature under reaction conditions. Four different irradiation environments were considered for this study: (i) visible light, (ii) ultraviolet light, (iii) simulated solar irradiation (4% UV), and (iv) dark conditions (as a reference). Simulated solar irradiation was a theoretical approach to resemble sunlight, considering that the solar spectrum is integrated by 4% UV light, 43% visible light, and 53% near-infrared radiation. For experimental purposes, only UV and visible contributions were contemplated due to the equipment's capabilities.

Regarding reaction specifications, 25 mg of the photocatalyst was dispersed in 50 mL of the corresponding RhB solution (10 ppm unless otherwise stated). Initially, the sample was stirred in the dark for 30 min to establish the adsorption/desorption equilibrium between the catalyst and RhB (amount of Rhodamine adsorbed). Once equilibrium was reached, the lamps were turned on under the desired irradiation conditions, and the photocatalytic reaction was monitored for 120 min. At this point, it is important to highlight that RhB did not degrade when the solution was irradiated in the absence of a catalyst (photolysis). During photocatalysis, aliquots were collected at regular intervals and centrifuged at 4000 rpm for 10 min to separate the catalyst. In all cases, the amount of RhB in solution was analyzed using an HPLC equipment Shimadzu SCL-40 Nexera Series equipped with a photodiode array (PDA) detector (RhB, 554 nm) and a C18 reversed-phase column. The mobile phase was a mixture of methanol and water (70:30, v/v) at a flow rate of 1.0 mL/min. Additional identification analyses were performed using a high-performance liquid chromatography system (HPLC; Agilent, model 1100 series) coupled to a variable wavelength visible-UV detector and an ion trap mass spectrometer (Agilent model 1100 Series LC/MSD Trap SL).

Concentration values obtained were used to calculate the RhB photodegradation rate according to the following equation:

$$Degradation\ rate\ (\%) = \left(\frac{C_0 - C_i}{C_0}\right) \bullet 100\ \% \qquad [1]$$

In the final step of this study, the most efficient photocatalysts were tested under high concentration loads (20–50 ppm range), maintaining the previously stated conditions (i.e., 25 mg of catalyst in 50 mL of the RhB aqueous solution). These tests were performed under simulated solar irradiation and using dark conditions in the first minutes to identify the adsorption capacity. Finally, a cycling experiment was also designed to evaluate the durability of the most promising catalyst (TiO_2/SWCNTs) against the reference material TiO_2 P25. More specifically, these cyclability tests were performed with a 20 ppm RhB aqueous solution until complete degradation under UV irradiation, followed by consecutive regenerations of the original 20 ppm RhB solution without any manipulation of the photocatalysts (through the incorporation of 3 mL (aliquots removed for analysis) of a more concentrated RhB solution to recover 50 mL aqueous solution with 20 ppm RhB).

3. Results and discussion

3.1. Physicochemical characterization of the synthesized photocatalysts

The textural properties of the selected carbon nanostructures and their associated TiO_2-based composites were evaluated using N_2 adsorption/desorption measurements at cryogenic temperatures. Isotherms before and after modification with TiO_2 are described in Fig. 1A & B, while textural parameters for the synthesized photocatalysts are reported in Table 1. In general, all the carbons evaluated are non-porous in nature (adsorption isotherms are rather flat), except single-walled carbon nanotubes (SWCNTs) and partially reduced graphene oxide (prGO). These two samples constitute an exception and exhibit a significant knee in the nitrogen isotherm at low relative pressures. The sharp knee below $p/p_0 < 0.02$ clearly reflects the presence of narrow and uniform micropores in both samples. Additionally, these two materials exhibit a significant nitrogen condensation above $p/p_0 \approx 0.7$ due to the presence of cavities or voids in the mesoporous range. These mesocavities do not necessarily reflect a well-developed inner porous structure but rather correspond to nitrogen adsorption in the interparticle space or in the space between the tube bundles in the case of CNTs (García Blanco et al., 2011). Original TiO_2 P25 is also non-porous with a rather flat adsorption profile. Upon wet impregnation of the carbon nanostructures with TiO_2 (90 wt%), the adsorption performance changes significantly, preferentially for samples TiO_2/SWCNT and TiO_2/prGO. These two samples exhibit a significant blocking of the micro- and mesoporous structure due to the incorporation of the TiO_2 nanoparticles. These results confirm the successful dispersion of the carbon nanostructures within the titania matrix. BET surface area ranges from ca. 50–55 m^2/g in pure TiO_2, gCN- and GI-based composites, slightly increasing for the two composites made with porous carbon materials, i.e., TiO_2/prGO (85 m^2/g) and TiO_2/SWCNT (120 m^2/g). In any case, these values are much smaller than those in the original carbons (e.g., 647 m^2/g and 843 m^2/g for prGO and SWCNT, respectively). These differences cannot be exclusively attributed to the occluding of the porosity by TiO_2 but also to the additional weight (90 wt%) of the non-porous TiO_2 in the composites.

Table 1
Textural properties of the composites obtained from the nitrogen adsorption data after application of the BET and Dubinin-Radushkevich equations.

Sample	S_{BET} (m^2/g)	Total Pore Volume (cm^3/g)	Mesopores Volume (cm^3/g)	Micropores Volume (cm^3/g)
TiO_2/gCN	56	0.45	0.43	0.02
TiO_2/GI	55	0.37	0.36	0.01
TiO_2/prGO	85	0.55	0.52	0.03
TiO_2/SWCNT	120	0.49	0.45	0.04
TiO_2 P25	57	0.25	0.23	0.02

The crystallographic structure of the photocatalysts and their pure components was evaluated using X-ray diffraction measurements (XRD). Fig. 2A confirms the combined presence of anatase and rutile phases in the commercial TiO_2 P25 sample (Jiang et al., 2018). As expected, the carbon nanostructures selected for this study (Fig. 2B) do not exhibit significant crystallographic features, except sample GI with a marked contribution at 26.5°, associated with the (002) diffraction peak of graphite, and sample gCN with a small contribution at 27.4°, associated with the (002) diffraction contribution of C_3N_4 due to the interlayer stacking of aromatic units (Al-Hajji et al., 2019; Fina et al., 2015; Li

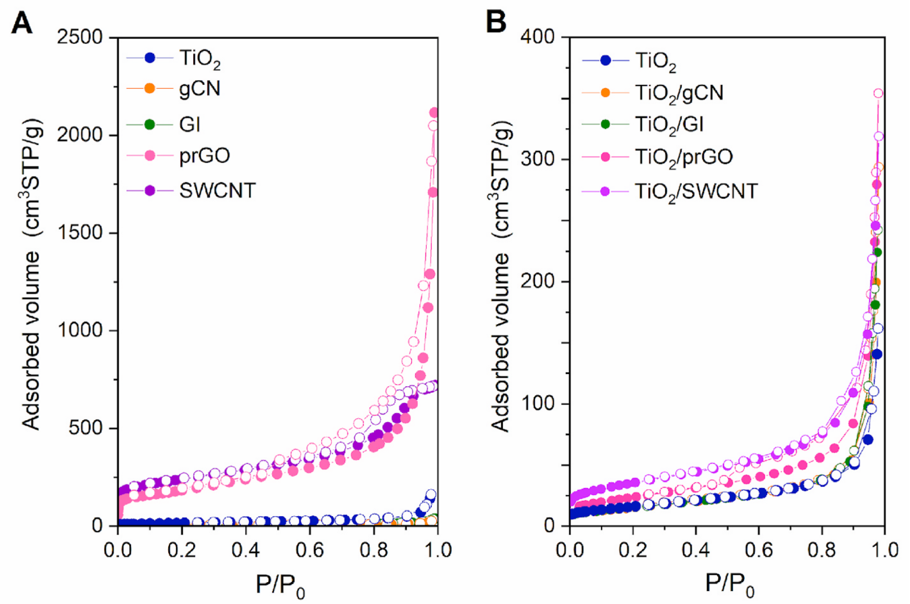

Fig. 1. N_2 adsorption/desorption isotherms at −195 °C for (**A**) the different carbon supports evaluated and (**B**) the corresponding TiO_2-based photocatalysts. TiO_2 P25 has been added to both figures for comparison.

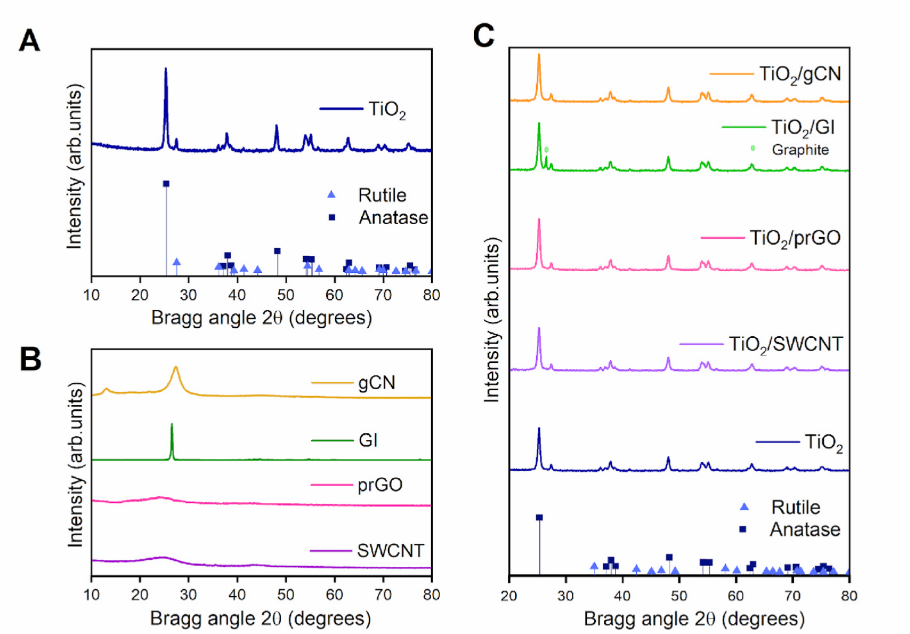

Fig. 2. XRD pattern for (A) commercial TiO_2 P25, (B) carbon nanostructures evaluated, and (C) synthesized photocatalysts.

et al., 2007). The composites (Fig. 2C) exhibit the characteristic pattern of TiO_2 with peaks at 25.4°, 37.7°, 48.1°, 53.9°, 55.1°, and 62.8°, corresponding to the (101), (004), (200), (105), (211) and (204) crystal planes of TiO_2. The average crystal size for TiO_2 estimated from the Scherrer equation is rather similar for all samples and ranges from 20 nm for pristine TiO_2 P25 to 17–19 nm for the composites. Overall, the absence of significant changes in the XRD pattern (peak position and intensity) in the composites anticipates a similar crystallographic

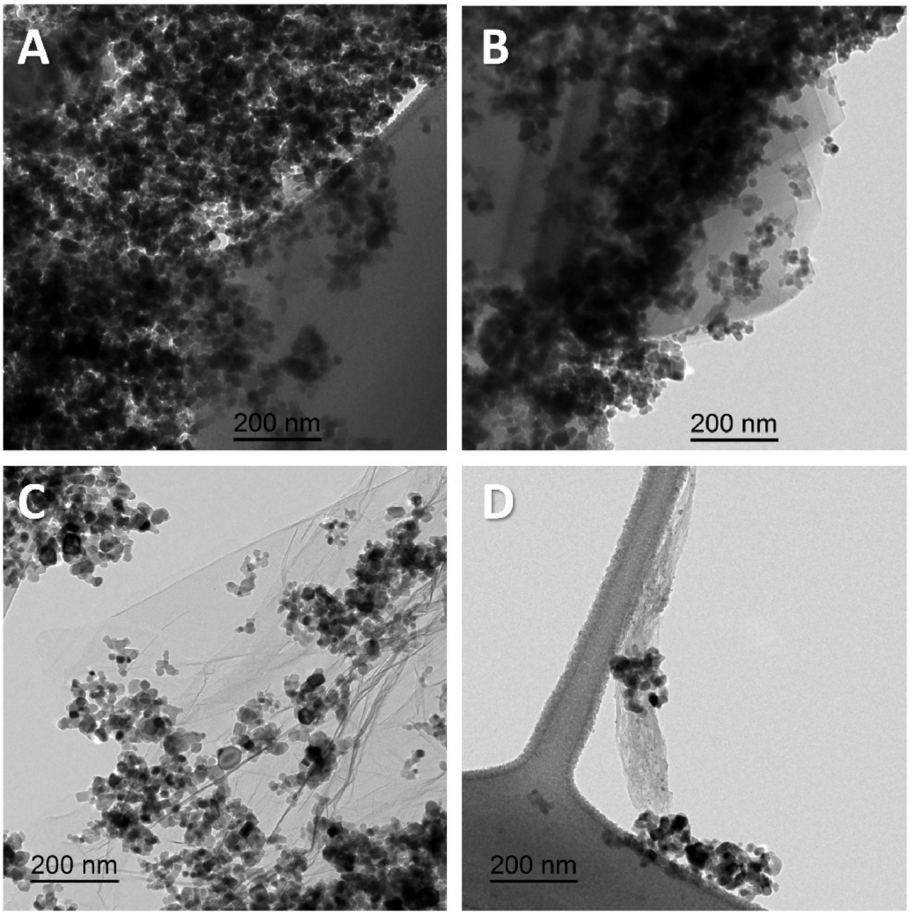

Fig. 3. TEM images of samples (A) TiO_2/gCN, (B) TiO_2/GI, (C) TiO_2/prGO, and (D) TiO_2/SWCNT composites.

structure for all photocatalysts, independently of the carbon platform incorporated.

Transmission electron microscopy images (Fig. 3) of the composites constitute a useful tool to get insights into the dispersion of the TiO_2 nanocrystals and the carbon additives, including the formation of proper heterojunctions. As it can be observed in Fig. 3, TiO_2 particle size is rather similar among samples (ca. 15–20 nm), in close agreement with the XRD measurements. In general, the dispersion of the TiO_2 nanocrystals is relatively good for all catalysts evaluated (more effective in the case of the C_3N_4 support), except for the SWCNT-based sample, where non-uniform aggregates can be appreciated. Furthermore, TEM images confirm the lamellar structure of GI and prGO with irregular wrinkles and the bundled structure of tubular single-walled carbon nanotubes. In summary, TEM images confirm the successful dispersion of TiO_2 nanocrystals in the carbon supports, in close agreement with nitrogen adsorption data, and the success in the development of proper oxide-carbon heterojunctions at the interface.

XPS spectra of the synthesized composites and the non-modified TiO_2 P25 are displayed in Fig. 4. Additional details about the XPS peaks are summarized in Table S1. The Ti 2p core spectra of the bare TiO_2 P25 exhibit two well-defined contributions at 458.1 eV and 463.8 eV, corresponding to Ti $2p_{3/2}$ and Ti $2p_{1/2}$, respectively. These contributions clearly reflect the presence of Ti^{4+} oxidation state, in close agreement with the literature (Yu et al., 2017; Zhao et al., 2022). The binding energy difference between both peaks (5.7 eV) validates the assigned valence state. The O1s spectrum is mainly composed of a sharp contribution at 529.3 eV, typically assigned to lattice oxygen (Ti–O bond) (Yu et al., 2017; Zhao et al., 2022). Interestingly, a significant

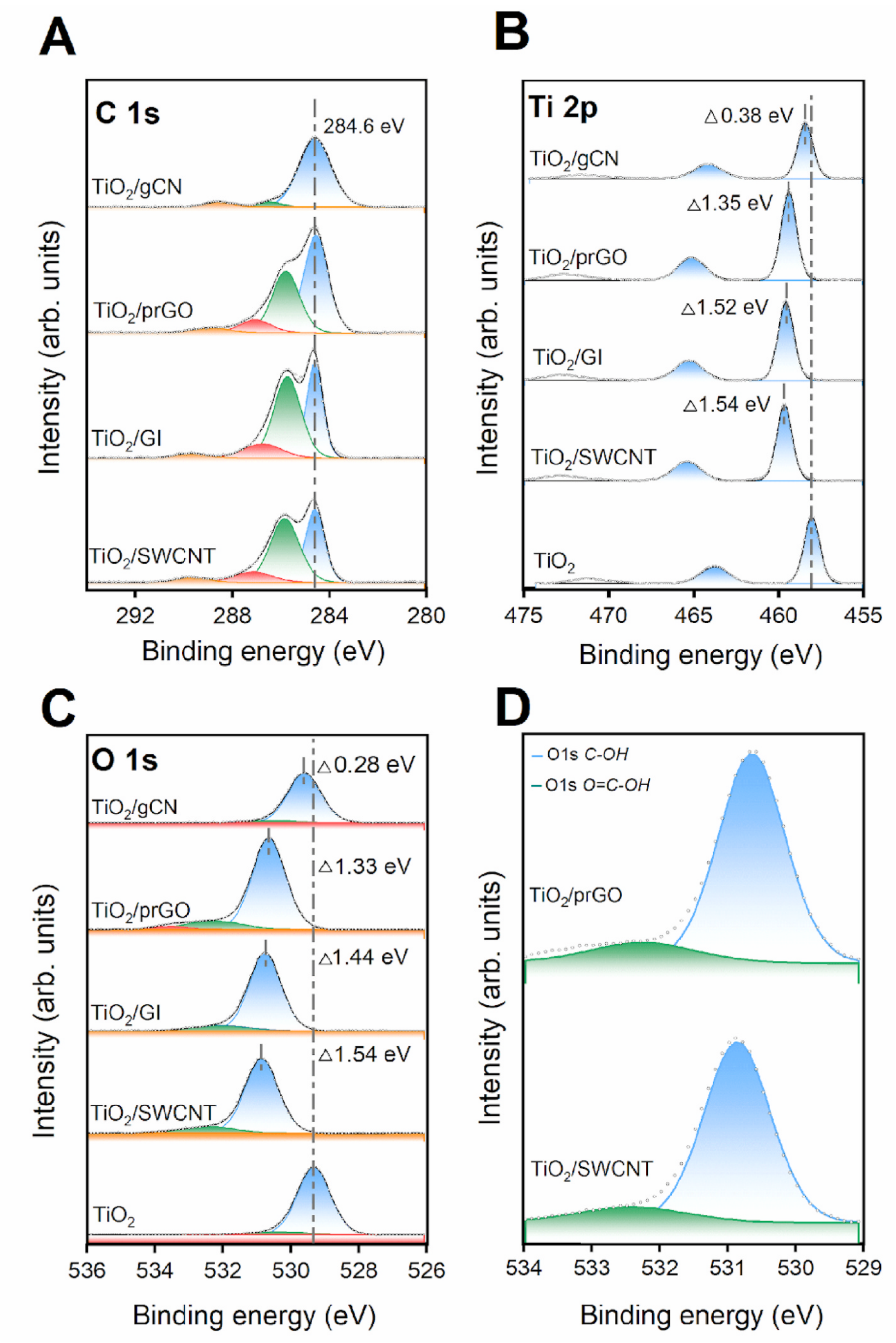

Fig. 4. XPS spectra of composites and pristine TiO_2 P25 for: a) C 1s, b) Ti 2p, c) O 1s, and d) magnified O1s core level.

shift for both Ti 2p and O 1s contributions is observed in the composites, these shifts being more significant for samples TiO_2/prGO and TiO_2/SWCNT. A shift to higher binding energies suggests the formation of slightly electron-deficient Ti^{4+} centers, most probably due to the transfer of electron density from the TiO_2 nanocrystals to the “highly conductive” carbon supports. At this point, it is important to highlight that these signals are below the binding energy for Ti^{3+} in Ti_2O_3 (ca. 461 eV), thus excluding the presence of Ti^{3+} species (Doan Nguyen et al., 2022). The modified electronic structure upon carbon incorporation anticipates the presence of strong oxide-carbon interactions in the newly formed heterojunctions. As claimed above, the most significant shift is observed for sample TiO_2/SWCNT (ca. 1.54 eV), followed by TiO_2/GI (ca. 1.52 eV), TiO_2/prGO (ca. 1.35 eV), and finally TiO_2/gCN (ca. 0.38 eV). These results agree with the higher conductivity and charge carrier mobility of SWCNTs, high conductivity graphite flakes, and graphene, as compared to the semiconducting character of the 2D graphitic carbon nitride (Wang et al., 2017; Marinho et al., 2012). A similar displacement is observed in the O 1s spectra. The blue shift is larger for sample TiO_2/SWCNT with binding energy for the O 1s peaks at 530.9 eV and a shoulder at 532.4 eV. The small contribution at 532.4 eV could be associated with O═C–OH and C–OH bonds. Interestingly, both contributions are affected by the changes in electron density of the oxygen species in TiO_2 due to the strong oxide/support interactions at the interface. For the C 1s signal, all composites exhibit four contributions, the most intense peaks at ca. 284.6 eV and 285.8 eV, associated with sp^2 C═C and sp^3 C–C bonds, respectively, followed by small contributions at 287.1 eV and 288.9 eV, due to different surface carbon-oxygen species (Tian et al., 2011; Doan Nguyen et al., 2022). Overall, these observations open the gate towards an improved photocatalytic behavior of the composites due to the acceptor character of the selected carbon nanostructures for photogenerated electrons at the TiO_2 nanoparticles, thereby anticipating an improved charge-separation efficiency, with the associated delay in the electron-hole recombination (An et al., 2011). Doan Nguyen et al. observed a similar blue shift in the $Ti^{4+}2p_{3/2}$ signal for graphene oxide on TiO_2 under UV irradiation (Doan Nguyen et al., 2022). These observations were ascribed to the formation of Ti–O–C bonds in the irradiated samples. Sher Shah et al. ascribed these blue shifts to the interactions of Ti with the oxygen functionalities in the carbon, i.e., highly electronegative oxygen species in the carbon network withdraw electron density from Ti (Sher Shah et al., 2012). Our results confirm the presence of strong oxide-carbon interactions at the formed heterojunction, associated with significant changes in the electronic density. However, the absence of an XPS C1s contribution below 284 eV excludes the formation of Ti–C bonds at the interface (Tian et al., 2011; Doan Nguyen et al., 2022). XPS analysis also provides valuable information about the atomic percentage of the constituent species. Although on a mass basis, all composites were prepared with 90 wt% TiO_2 and 10 wt% carbon, at atomic percentage, these numbers translate into a 40 C1s/20 Ti2p atomic ratio.

To further explore the structural properties at the interface, the synthesized photocatalysts were analyzed using Raman spectroscopy (Fig. 5). All photocatalysts display essentially the same pattern as pristine TiO_2 P25 with the characteristic peaks at 135.5, 392.5, 507.5, and 631.5 cm^{-1}, corresponding to $E_g(1)$, $B_{1g}(1)$, $A_{1g} + B_{1g}(2)$, and $E_g(2)$, respectively (Balachandran et al., 1982). A closer look at the $E_g(1)$ contribution shows a shift to higher energies for samples TiO_2/SWCNT, TiO_2/GI, and TiO_2/prGO of 7, 8, and 9 cm^{-1}, respectively, compared to pristine TiO_2 P25. The observed shift constitutes another evidence of the modification of the vibrational energy of the titania crystal lattice after the incorporation of the carbon matrices due to the presence of strong interactions at the interface (strengthening of the Ti–O bond would agree with a deficiency in the electronic density of Ti centers upon carbon incorporation). Additional peaks related to structural disorders in carbon (D) and graphitic (G) features are also present in TiO_2/prGO and TiO_2/SWCNT composites, the latest one with higher intensity (Dresselhaus et al., 2010). In the case of TiO_2/prGO, the D band is located at 1346.5 cm^{-1}, and the G band at 1581.5 cm^{-1}, with an I_D/I_G ratio equal to 0.87. For TiO_2/SWCNT, the D band is centered at 1325.5 cm^{-1}, the G band at 1581.5 cm^{-1}, and a G’ band appeared at 2641.5 cm^{-1} with an I_D/I_G ratio equal to 0.12, characteristic of SWCNTs (Costa et al., 2008). These findings confirm previous XPS results and support the hypothesis about the presence of strong oxide/support interactions at the interface, thus opening the gate to an unexplored photocatalytic performance.

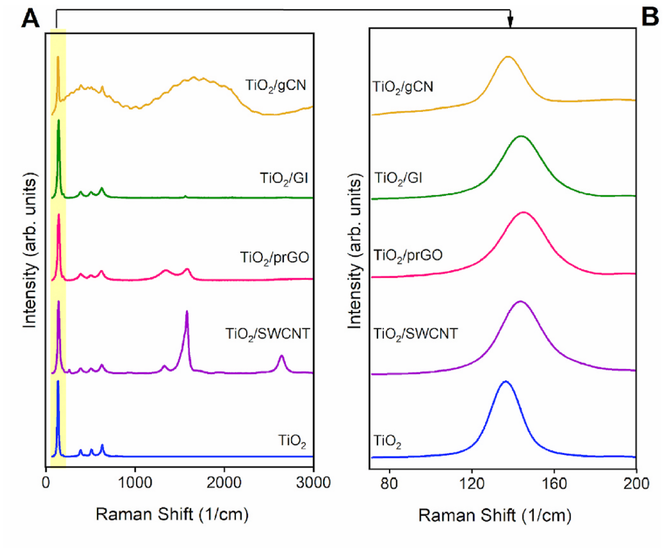

Fig. 5. Raman shifts for the evaluated photocatalysts. (Inset) Magnification of the 80-200 cm^{-1} range.

3.2. Band structure analysis

The energy gap and band structure of the synthesized photocatalysts were evaluated before testing their photocatalytic performance. These intrinsic properties are crucial to understanding their subsequent performance in photo-degradation processes. The band gap of the composites was estimated according to the Kubelka-Munk function and Tauc method based on the diffuse reflectance spectra (Makula et al., 2018). General steps consisted of reflectance data normalization (Eq. (2)), implementing the Kubelka-Munk equation (Eq. 3), conversion to eV unit (Eq. (4)), and applying the Tauc method considering the nature of the semiconductors (direct or indirect) (Eq. (5)).

$$R_N = \frac{R_i}{R_{max}} \qquad [2]$$

$$f(R_N) = \frac{(1 - R_N)^2}{2R_N} \qquad [3]$$

$$E_{eV} = \frac{1\ eV \bullet E_{Joule}}{(1.6E - 19)_{Joule}} = \frac{1\ eV \bullet ((h \bullet c)/\lambda_i)_{Joule}}{(1.6E - 19)_{Joule}} \qquad [4]$$

$$\begin{aligned} Tauc\ Method\_Direct &= (f(R_N) \bullet E)^2 \\ Tauc\ Method\_Indirect &= (f(R_N) \bullet E)^{1/2} \end{aligned} \qquad [5]$$

Some of the variables employed were h as the Plank’s constant ($6.63 \bullet 10^{-34}$ J/s), c representing light velocity ($3 \bullet 10^8$ m/s), and λ is the wavelength according to diffused reflection spectra (DRS) data, with the corresponding unit arrangement. Once plotted, *Photon energy-vs-Tauc eq.*, an extrapolation of the straight segment of the curve to the abscissa axis gave the band gap energy (E_g), as shown in Fig. S1A. Valence band position was obtained using ultraviolet photoelectron spectroscopy (UPS) as an XPS at low photon energy. In this case, the extrapolation of the curve’s linear portion toward the *X*-axis provided the valence band maximum, as shown in Fig. S1B. Combining UPS and DRS results enables the estimation of the conduction band.

Based on the above analysis, the band structure of the composites was determined, as displayed in Fig. 6. However, optical features are material intrinsic properties and, therefore, are not strict values. In fact, several studies have reported the dependence of energy gap and band position on the synthesis method and conditions, among others (Seo et al., 2013; Singh et al., 2015).

Titanium dioxide, the major component of the composites, shows a typical 3.3 eV band gap with a maximum valence band positioned at 2.9 eV (NHE); meanwhile, the conduction band minimum was found at −0.4 eV. However, once the TiO_2 is modified with the carbon supports, a significant change in the band gap is observed, i.e., a reduced band gap is observed for composites (Hajialilou et al., 2021). The reduction trend in the band gap was TiO_2/gCN (3.2 eV) < TiO_2/GI (2.6 eV) < TiO_2/prGO (2.7 eV) < TiO_2/SWCNT (2.56 eV) (Table S2). The observed tendency implies an expansion of the photo-responsive spectra towards visible light in the composites, preferentially for highly conductive carbon nanostructures, thus anticipating a potential effect of the carbon modifier in the photocatalytic performance of TiO_2. Along with these shifts, the valence band (VB) suffered a reduction while the conduction band (CB) was increased, which, according to Shehzad et al., could indicate strong interactions between the carbon species and TiO_2, in close agreement with previous XPS and Raman results described before (Shehzad et al., 2018).

3.3. Photocatalytic performance

Rhodamine B was selected as a model pollutant to evaluate the photocatalytic activity of TiO_2/carbon photocatalysts due to its stable nature, providing a benchmark for determining the effectiveness of these materials. The photocatalysts were tested under four different lighting conditions, i.e., ultraviolet, visible, simulated solar irradiation, and darkness (to reference the adsorption process). After 30 min in the dark (once equilibrium had been reached), samples were exposed to irradiation, and the photocatalytic conversion was evaluated over time. Fig. 7 shows all the conversion profiles for the four evaluated photocatalysts, including TiO_2 P25 as a reference.

As described above, photocatalytic tests performed in dark conditions were used to identify the potential of the composites to remove RhB exclusively by physisorption. Fig. 7A shows that 30 min in solution is sufficient to reach equilibrium, independently of the composite evaluated. Under the experimental conditions tested, samples TiO_2/prGO and TiO_2/SWCNT are able to remove RhB to a high extent, removal capacity >70% and >90%, respectively, exclusively through adsorption processes. These results are in close agreement with the large BET surface area described above for these samples and their intrinsic textural properties (presence of micro and mesopores). The photocatalytic profiles remain similar under UV, visible, and simulated solar irradiation (Fig. 7B–D), with samples TiO_2/prGO and TiO_2/SWCNT outperforming the other tested materials, including TiO_2 P25. The improved performance in the composites must be attributed to the dual mechanism for Rhodamine B (RhB) removal, i.e., simultaneous adsorption and degradation. More specifically, under visible light, the most promising performance is achieved with sample TiO_2/SWCNT, with nearly 100% RhB removal in 60 min. Under similar conditions (60 min reaction time), sample TiO_2/prGO is able to remove >80% of the dye, while TiO_2/gCN, TiO_2/GI, and pristine TiO_2 P25 have a poor performance (removal efficiency <40%). The photocatalytic performance of the composites improves under simulated solar light (Fig. 7C) due to the incorporation of some UV irradiation, whereas the best performance is achieved when exclusively UV light is used (Fig. 7D), preferentially for samples TiO_2/gCN, TiO_2/GI, and pristine TiO_2 P25. Under these irradiation conditions, all tested photocatalysts are able to remove >90% RhB after 60 min. In any case, samples TiO_2/prGO and TiO_2/SWCNT are the most promising photocatalysts due to their dual functionality, adsorption, and photocatalytic degradation, thus outperforming the widely applied TiO_2 P25 photocatalyst. These results open the gate towards the application of these carbon-based composites in wastewater treatment plants with contamination spikes. The dual mechanism can provide a first barrier to remove high concentration spikes through adsorption in the carbon modifier, followed by photocatalytic degradation by the nearby TiO_2 active sites. In any case, the observed findings clearly emphasize the promoting role of the carbon additive (with only 10 wt%) in the photocatalytic performance, overpassing pure TiO_2 P25.

To further explore the promoting role of carbon nanostructures in the photocatalytic performance of TiO_2 P25 and the benefits of the dual mechanism, similar tests were performed with samples TiO_2 and TiO_2/SWCNT, but under highly demanding reaction conditions (RhB concentration was increased up to 50 ppm). Higher contaminant loads saturate SWCNTs faster, thus allowing a better comparison of the photocatalytic performance of pristine and modified TiO_2 P25. Fig. 8A

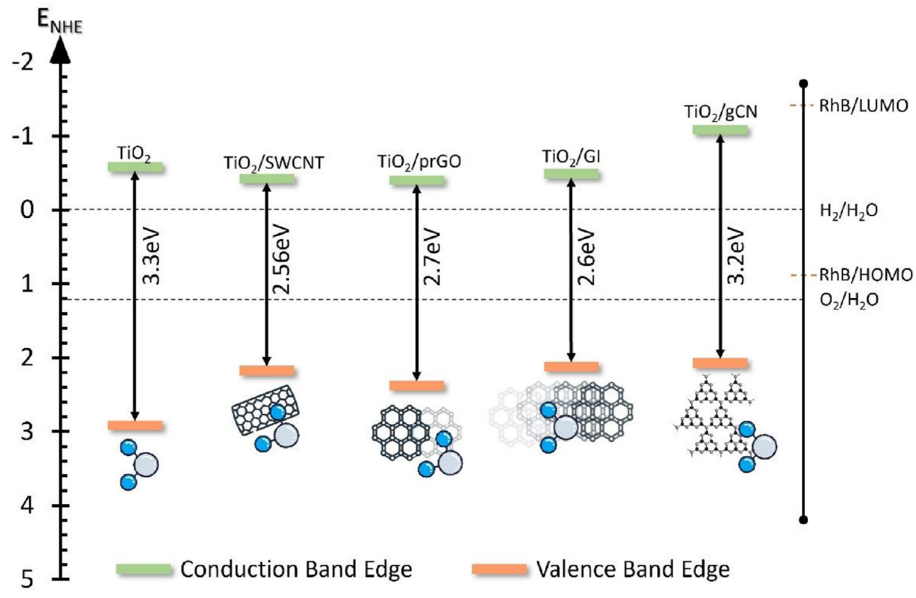

Fig. 6. Schematic representation of composite's electronic properties.

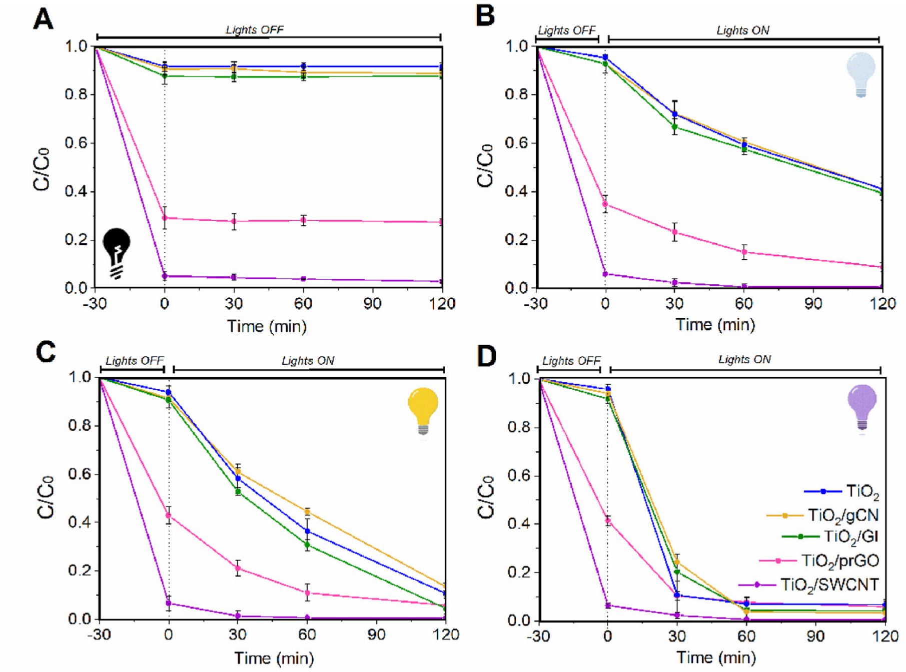

Fig. 7. Photocatalytic conversion of RhB versus reaction time for the five catalysts evaluated (pristine TiO_2 (P25), TiO_2/gCN, TiO_2/GI, TiO_2/prGO, and TiO_2/SWCNT) under four different lighting environments: a) dark, b) visible, c) solar simulation, and d) UV. Photocatalytic tests were performed at 25 °C using a RhB concentration of 10 ppm (see experimental section for further details). Error bars are included.

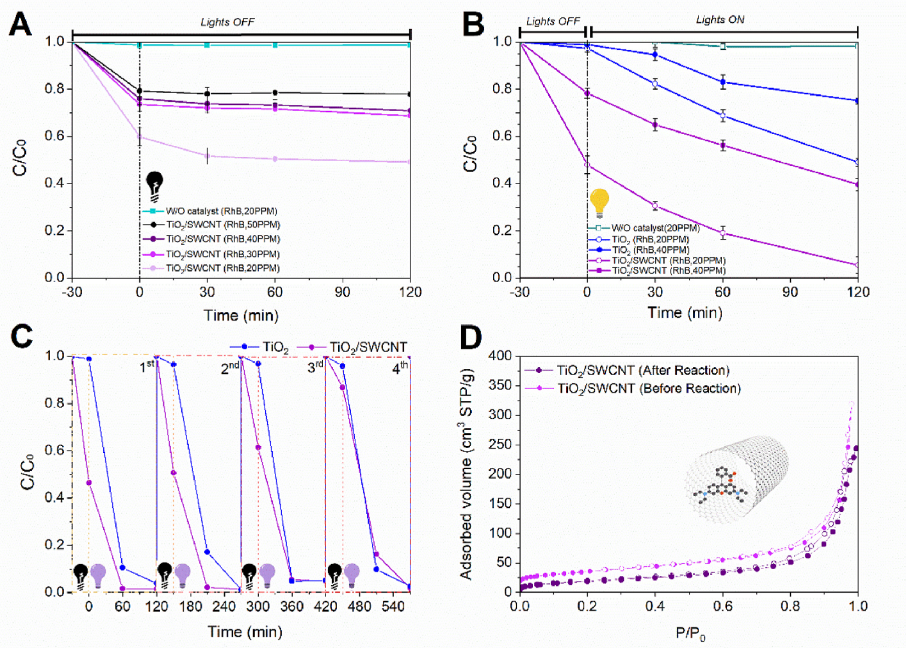

Fig. 8. A Evaluation of the adsorption performance of sample TiO_2/SWNCT for Rhodamine B at different concentrations, **B** Photocatalytic performance of samples TiO_2 and TiO_2/SWNCT at different initial concentrations and using simulated solar irradiation. Experiments without catalyst are included to exclude the effect of irradiation (photolysis) in the photocatalytic performance, **C** Catalyst cyclability assessment under UV irradiation (TiO_2/SWNCT), and **D** Nitrogen adsorption/desorption isotherms for the original and used TiO_2/SWNCT photocatalyst.

compares the adsorption performance for TiO_2/SWCNT in dark conditions and under different RhB concentrations. Experimental results show that the adsorption capacity of TiO_2/SWCNT remains quite high, even at an initial concentration of 20 ppm, while this quantity diminishes at 30 ppm and above due to the saturation of the inner cavities in the nanotubes. Fig. 8B compares the photocatalytic performance of the pristine TiO_2 P25 and the carbon-modified TiO_2/SWCNT sample in two different initial concentrations, 20 and 40 ppm, under simulated solar irradiation. Even under these demanding reaction conditions, TiO_2/SWCNT outperforms sample TiO_2 with more than 90% RhB removal after 120 min and 20 ppm; and 50% RhB removal after 120 min and 40 ppm. Under similar reaction conditions, the well-known TiO_2 P25 photocatalyst can only remove 42% and 20%, respectively. These results confirm the improved adsorption/photocatalytic performance of SWCNT-modified

TiO_2 photocatalysts.

Another important aspect to be considered in photocatalysis is the potential of the synthesized photocatalysts to work under consecutive cycles (cyclability tests). To test the long-term stability/durability of these materials, TiO_2 P25 and TiO_2/SWNCT photocatalysts have been evaluated in four consecutive cycles using fresh RhB (20 ppm) in each of these cycles. More specifically, the reaction tests were performed using 25 mg of catalyst dispersed in a 50 mL RhB solution under UV-light for fast response. Fig. 8C demonstrates that both photocatalysts remain stable after four consecutive cycles with a very promising performance (ca. 100% removal in 120 min). However, a closer look at the catalytic profile of sample TiO_2/SWNCT shows that the dual performance described above (combining adsorption and photocatalysis) decreases after each cycle, most probably due to the irreversible blocking of the microporosity in SWCNTs by non-reacted RhB. To further test this hypothesis, nitrogen adsorption measurements have been performed in the original and the recovered sample (Fig. 8D). Nitrogen adsorption data clearly shows that the recovered sample exhibits a significant decrease in the nitrogen adsorption performance, mainly in the low relative region, after use. Total pore volume diminishes from 0.49 cm^3/g in the as-synthesized sample, down to 0.28 cm^3/g after reaction. This finding anticipates that the regeneration of the inner tubular space of the CNTs is not an easy task due to the preferential adsorption of non-reacted RhB. Further experiments are needed to identify novel regeneration conditions able to degrade confined RhB species.

3.4. *Photocatalytic mechanism*

The photocatalytic mechanism for Rhodamine-B degradation may vary depending on the specific carbon nanostructure evaluated (Fig. 9). However, several studies in the literature converge on a standard photocatalytic mechanism, where the carbon structure acts as a sink for electrons, therefore retarding the recombination rate between electrons and holes (Nguyen et al., 2016; Raja et al., 2019). Particularly, Nguyen et al. demonstrated using DFT calculations that the remarkable effectiveness associated with SWCNTs incorporated into the TiO_2 matrix is attributed to the trapping of electrons at the interface. Theoretically, when a semiconductor material is irradiated with sufficient energy (light), exceeding its band gap, electrons (e^-) are excited from the valence band to the conduction band. This transition creates positively charged vacancies in the valence band, known as holes (h^+). The critical point in photocatalysis is to achieve an efficient electron-hole separation and to minimize their recombination rate. The photogenerated electrons and holes interact with water molecules and dissolved oxygen, thus giving rise to reactive oxygen species (ROS) (i.e., O2-·, OH·) (Gunnagol et al., 2018). These radicals are strong oxidizers capable of degrading complex organic molecules like RhB by successive reactions. Eventually, this dye undergoes a series of transformations through different intermediates, depending on the degradation path, ultimately resulting in its complete mineralization into CO_2 and H_2O (Chen et al., 2021).

Additional HPLC-mass spectrometry analyses were performed to identify the degradation products formed under reaction conditions. The degradation of this xanthene dye can proceed through various pathways, and the identification of the generated intermediates is crucial to understanding the reaction mechanism (Rasalingam-Peng et al., 2015). Under reaction conditions, two main peaks were identified for the TiO_2/SWCNT system, Rhodamine B ($m/z = 442$) and N,N-diethyl-N′-ethylrhodamine (DER) ($m/z = 415$), due to the elimination of a single ethyl group (Bhooma et al., 2020; Siwińska-Ciesielczyk et al., 2020). Additionally, tinny peaks appear at $m/z = 387$, associated with another de-ethylation fragment (N,N-diethylrhodamine, DR and/or N-ethyl-N′-ethylrhodamine, EER), related to a possible cleavage of the C–O bond in the aromatic ring (Xiao et al., 2019; Rasalingam-Peng et al., 2015). Another de-ethylation of the parent compound coupled with the addition of an –OH group is confirmed by a peak at 431 m/z (Rasalingam-Wu et al., 2015). Moreover, hydroxylation and oxidation intermediates were confirmed by ions at $m/z = 459$ and 477, respectively (Zhang et al., 2018; Siwińska-Ciesielczyk et al., 2020). Overall, these results suggest that the degradation of Rhodamine-B proceeds via the N-deethylation mechanism (Xiao et al., 2019; Rasalingam-Peng et al., 2015). However, the small concentration of these reaction intermediates suggests that the evaluated photocatalysts preferentially promote mineralization to CO_2 and H_2O.

4. Conclusions

Integrating TiO_2 into carbon nanostructures such as SWCNTs and prGO significantly enhances their textural characteristics, notably increasing surface area and pore volume, as evidenced by nitrogen adsorption/desorption studies. XRD and TEM analyses corroborate the effective dispersion of TiO_2 nanoparticles within these carbon matrices, leading to the formation of efficient oxide/carbon heterojunctions. Furthermore, XPS and Raman spectroscopy analyses indicate strong interactions between oxide and the carbon components, decreasing band gap energy from 3.3 eV for TiO_2 to 2.56 eV for TiO_2/SWCNT. This band gap narrowing is associated with improved photocatalytic efficiency, increasing from an estimated 17%–45% within just 60 min under solar irradiation (40 ppm RhB solution), owing to enhanced charge separation and diminished electron-hole recombination. These findings highlight the potential of TiO_2/carbon heterojunctions for innovative applications in energy conversion and environmental remediation.

The dual functionality of these materials for adsorption and

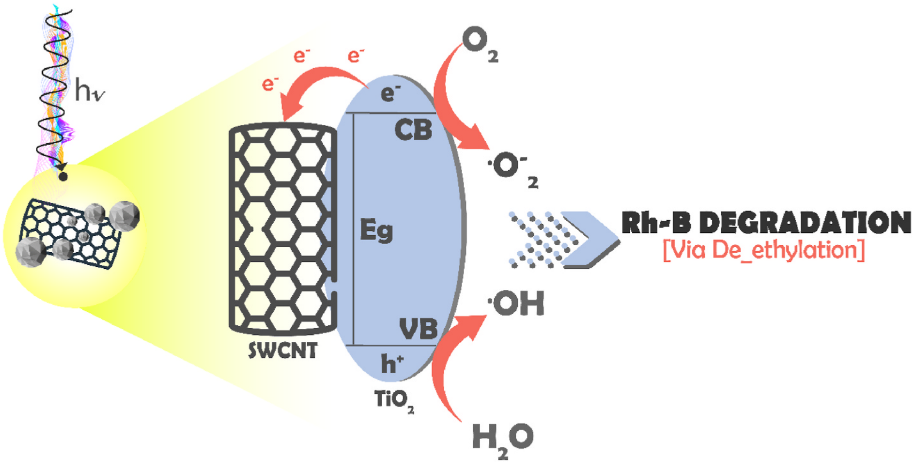

Fig. 9. Proposed mechanism for RhB photodegradation using TiO_2/SWCNT catalyst.

photocatalysis simultaneously, particularly under conditions of high pollutant concentration, positions them as promising candidates for wastewater treatment technologies. Nonetheless, the reduction in adsorption capacity and pore volume after repeated cycles presents a challenge in regenerating these photocatalysts. Therefore, while carbon-modified TiO_2 photocatalysts surpass traditional TiO_2 P25 in terms of immediate efficacy, further research into their long-term stability and reusability is essential to realize their potential for practical applications fully. Ultimately, this research delivers a thoughtful comparison of the most cited carbon materials, elucidating the necessity to recognize the multifaceted nature of carbon materials in photocatalytic applications.

CRediT authorship contribution statement

C. Abreu-Jaureguí: Writing – original draft, Investigation, Formal analysis, Conceptualization. **L. Andronic:** Supervision, Resources, Conceptualization. **A. Sepúlveda-Escribano:** Supervision, Conceptualization. **J. Silvestre-Albero:** Writing – review & editing, Supervision, Project administration, Methodology, Funding acquisition, Conceptualization.

Declaration of competing interest

The authors declare that they have no known competing financial interests or personal relationships that could have appeared to influence the work reported in this paper.

Data availability

Data will be made available on request.

Acknowledgements

Authors acknowledge financial support from MINECO (PID2019-108453 GB-C21) and MCIN/AEI/10.13039/501100011033 and EU “NextGeneration/PRTR (Project PCI2020-111968/ERANET-M/3D-Photocat), and Conselleria de Innovación, Universidades, Ciencia y Sociedad Digital (Project CIPROM/2021/022). L.A. acknowledges financial support from Romanian National Authority for Scientific Research and Innovation, CCCDI-UEFISCDI, Project number 169/2020 ERANET-M.-3D-Photocat.

Appendix A. Supplementary data

Supplementary data to this article can be found online at https://doi.org/10.1016/j.envres.2024.118672.

References

Al-Hajji, L.A., Ismail, A.A., Atitar, M.F., Abdelfattah, I., El-Toni, A.M., 2019. Construction of mesoporous g-C_3N_4/TiO_2 nanocrystals with enhanced photonic efficiency. Ceramics Int 45, 1265–1272. https://doi.org/10.1016/j.ceramint.2018.10.009.

Advanced oxidation processes for waste water treatment. In: Ameta, S.C., Ameta, R. (Eds.), 2018. Emerging Green Chemical Technology. Elsevier Inc., pp. 1–412. https://doi.org/10.1016/C2016-0-00384-4

An, X., Yu, J.C., 2011. Graphene-based photocatalytic composites. RSC Adv. 1, 1426–1434. https://doi.org/10.1039/c1ra00382h.

Balachandran, U., Eror, N.G., 1982. Raman spectra of titanium dioxide. J. Solid State Chem. 42, 276–282. https://doi.org/10.1016/0022-4596(82)90006-8.

Bhooma, V., Nagasathiya, K., Vairamani, M., Parani, M., 2020. Identification of Synthetic dyes Magenta III (New Fuchsin) and rhodamine B as common Adulterants in commercial Saffron. Food Chem. 309, 125793 https://doi.org/10.1016/j.foodchem.2019.125793.

Bukhov, N.G., 2004. Dynamic light regulation of photosynthesis (A review). Russian J. Plant Physiology 51, 742–753. https://doi.org/10.1023/B:RUPP.0000047822.66925.bf.

Chen, S., Ma, L., Du, Y., Zhan, W., Zhang, T.C., Du, D., 2021. Highly efficient degradation of rhodamine B by carbon nanotubes-activated persulfate. Separation and Purification Technology 256, 117788. https://doi.org/10.1016/j.seppur.2020.117788.

Costa, S., Borowiak-Palen, E., Kruszynska, M., Bachmatiuk, A., Kalenczuk, R.J., 2008. Characterization of carbon nanotubes by Raman spectroscopy. Materials Science – Poland 26, 433.

Dresselhaus, M.S., Jorio, A., Souza Filho, A.G., Saito, R., 2010. Defect characterization in graphene and carbon nanotubes using Raman spectroscopy. Phil. Trans. R. Soc. A 368, 5355–5377. https://doi.org/10.1098/rsta.2010.0213.

Doan Nguyen, T.T., Nguyen, D., Doan, H.N., Vo, P.P., Huynh, V.T., Hoang, V.H., Phan, T. B., Kinashi, K., Nguyen, P.T., 2022. In-depth understanding of the photoreduction of graphene oxide to reduced-graphene oxide on TiO_2 surface: Statistical analysis of X-ray photoelectron and Raman spectroscopy data. Appl. Surf. Sci. 581, 152325 https://doi.org/10.1016/j.apsusc.2021.152325.

European Food Safety (EFSA), 2005. Opinion of the Scientific Panel on Food Additives, Flavourings, Processing Aids and Materials in Contact with Food (AFC) to Review the Toxicology of a Number of Dyes Illegally Present in Food in the EU. EFSA Journal 3 (9), 263. https://doi.org/10.2903/j.efsa.2005.263.

Fina, F., Callear, S.K., Carins, G.M., Irvine, J.T.S., 2015. Structural investigation of graphitic carbon nitride via XRD and neutron diffraction. Chem. Mater. 27, 2612–2618. https://doi.org/10.1021/acs.chemmater.5b00411.

García Blanco, A.A., Rocha, J.V., Munera, J.F., Nazzarro, M., Zgrablich, G., Sapag, K., 2011. A study of the adsorption properties of single walled carbon nanotubes treated with nitric acid. Adsorption Sci. & Techn. 29, 705–722. https://doi.org/10.1260/0263-6174.29.7.705.

Gao, W., Wu, N., Du, J., Zhou, L., Lian, Y., Wang, L., Liu, D., 2016. Occurrence of rhodamine B contamination in capsicum caused by agricultural materials during the vegetation process. Food Chem. 205, 106–111. https://doi.org/10.1016/j.foodchem.2016.03.009.

Ghumro, S.S., Lal, B., Pirzada, T., 2022. Visible-light-driven carbon-doped TiO_2-based nanocatalysts for enhanced activity toward microbes and removal of dye. ACS Omega 7, 4333–4341. https://doi.org/10.1021/acsomega.1c06112.

Gunnagol, R.M., Rabinal, M.H.K., 2018. TiO2-Graphene nanocomposites for effective photocatalytic degradation of rhodamine-B dye. ChemistrySelect 3 (3), 2578–2585. https://doi.org/10.1002/slct.201703081.

Hajialilou, E., Asgharzadeh, H., Asl, ShK., 2021. TiO_2/rGO/Cu_2O ternary hybrid for high-performance photoelectrochemical applications. Appl. Surf. Sci. 544, 148832 https://doi.org/10.1016/j.apsusc.2020.148832.

Jiang, X., Manawan, M., Feng, T., Qian, R., Zhao, T., Zhou, G., Kong, F., Wang, Q., Dai, S., Pan, J.H., 2018. Anatase and rutile in evonik aeroxide P25: Heterojunctioned or individual nanoparticles? Catal. Today 300, 12–17. https://doi.org/10.1016/j.cattod.2017.06.010.

Kumar, S.G., Devi, L.G., 2011. Review of modified TiO_2 photocatalysis under UV/Visible light: selected results and related mechanisms on interfacial charge carrier transfer dynamics. J. Phys. Chem. A 115, 13211–13241. https://doi.org/10.1021/jp204364a.

Li, Z.Q., Lu, C.J., Xia, Z.P., Zhou, Y., Luo, Z., 2007. X-ray diffraction patterns of graphite and turbostratic carbon. Carbon 45, 1686–1695. https://doi.org/10.1016/j.carbon.2007.03.038.

Makula, P., Pacia, M., Macyk, W., 2018. How to correctly determine the band gap energy of modified semiconductor photocatalyts based on UV-vis spectra. J. Phys. Chem. Lett. 9, 6814–6817. https://doi.org/10.1021/acs.jpclett.8b02892.

Marinho, B., Ghislandi, M., Tkalya, E., Koning, C.E., de, G., 2012. With Electrical conductivity of compacts of graphene, multi-walled carbon nanotubes, carbon black, and graphite powder. Powder Techn 221, 351–358. https://doi.org/10.1016/j.powtec.2012.01.024.

Nguyen, K.C., Ngoc, M.P., Nguyen, M.V., 2016. Enhanced photocatalytic activity of Nanohybrids TiO2/CNTs materials. Mater. Lett. 165, 247–251. https://doi.org/10.1016/j.matlet.2015.12.004.

Ozawa, K., Emori, M., Yamamoto, S., Yukawa, R., Yamamoto, S., Hobara, R., Fujikawa, K., Sakama, H., Matsuda, I., 2014. Electron-hole recombination time at TiO_2 single-crystal surfaces: influence of surface band bending. J. Phys. Chem. Lett. 5, 1953–1957. https://doi.org/10.1021/jz500770c.

Raja, A., Selvakumar, K., Rajasekaran, P., Arunpandian, M., Ashokkumar, S., Kaviyarasu, K., Asath Bahadur, S., Swaminathan M, M., 2019. Visible active reduced graphene oxide loaded titania for Photodecomposition of Ciprofloxacin and its Antibacterial activity. Colloids Surf. A Physicochem. Eng. Asp. 564, 23–30. https://doi.org/10.1016/j.colsurfa.2018.12.024.

Rasalingam, S., Peng, R., Koodali, R.T., 2015a. An insight into the adsorption and photocatalytic degradation of rhodamine B in Periodic mesoporous materials. Appl. Catal. B Environ. 174–175, 49–59. https://doi.org/10.1016/j.apcatb.2015.02.040.

Rasalingam, S., Wu, C.-M., Koodali, R.T., 2015b. Modulation of pore sizes of titanium dioxide photocatalysts by a facile Template free Hydrothermal synthesis method: Implications for photocatalytic degradation of rhodamine B. ACS Appl. Mater. Interfaces 7, 4368–4380. https://doi.org/10.1021/am508883f.

Ren, G., Han, H., Wang, Y., Liu, S., Zhao, J., Meng, X., Li, Z., 2021. Recent advances of photocatalytic application in water treatment: a review. Nanomaterials 11, 1804. https://doi.org/10.3390/nano11071804.

Shehzad, N., Tahir, M., Johari, K., Murugesan, T., Hussain, M., 2018. Improved interfacial bonding of graphene-TiO_2 with enhanced photocatalytic reduction of CO_2 into solar fuel. J. Environm. Chem. Eng. 6, 6947–6957. https://doi.org/10.1016/j.jece.2018.10.065.

Sher Shah, M.S.A., Park, A.R., Zhang, K., Park, J.H., Yoo, P.J., 2012. Green synthesis of biphasic TiO_2-reduced graphene oxide nanocomposites with highly enhanced photocatalytic activity. ACS App. Mater. Interf. 4, 3893–3901.

Seo, S., Yoon, Y., Lee, J., Park, Y., Lee, H., 2013. Nitrogen-doped partially reduced graphene oxide rewritable nonvolatile memory. ACS Nano 7, 3607–3615. https://doi.org/10.1021/nn400588u.

Singh, M., Yadav, A., Kumar, S., Agarwal, P., 2015. Annealing induced electrical conduction and band gap variation in thermally reduced graphene oxide films with different sp^2/sp^3 fraction. Appl. Surf. Sci. 326, 236–242.

Siwińska-Ciesielczyk, K., Świgoń, D., Rychtowski, P., Moszyński, D., Zgoła-Grześkowiak, A., Jesionowski, T., 2020. The performance of Multicomponent oxide systems based on TiO2, ZrO2 and SiO2 in the photocatalytic degradation of rhodamine B: mechanism and Kinetic studies. Colloids Surf. A Physicochem. Eng. Asp. 586, 124272 https://doi.org/10.1016/j.colsurfa.2019.124272.

Skjolding, L.M., Jorgensen, L.vG., Dyhr, K.S., Köppl, C.J., McKnight, U.S., Bauer-Gottwein, P., Mayer, P., Bjerg, P.L., Baun, A., 2021. Assessing the aquatic toxicity and environmental safety of tracer compounds Rhodamine B and Rhodamine WT. Water Res. 197, 117109 https://doi.org/10.1016/j.watres.2021.117109.

Suyana, P., Ganguly, P., Nair, B.N., Pillai, S.C., Hareesh, U.S., 2021. Structural and compositional tuning in g-C_3N_4 based systems for photocatalytic antibiotic degradation. Chem. Eng. J. Adv. 8, 100148 https://doi.org/10.1016/j.ceja.2021.100148.

Tian, L., Ye, L., Deng, K., Zan, L., 2011. TiO_2/carbon nanotube hybrid nanostructures: Solvothermal synthesis and their visible light photocatalytic activity. J. Solid State Chem. 184, 1465–1471. https://doi.org/10.1016/j.jssc.2011.04.014.

Wang, X., Wang, F., Sang, Y., Liu, H., 2017. Full-spectrum solar-light-activated photocatalysts for light-chemical energy conversion. Adv. Energy Mater. 7, 1700473 https://doi.org/10.1002/aenm.201700473.

Xiao, X., Ma, X.-L., Liu, Z.-Y., Li, W.-W., Yuan, H., Ma, X.-B., Li, L.-X., Yu, H.-Q., 2019. Degradation of rhodamine B in a novel Bio-Photoelectric reductive system composed of Shewanella Oneidensis MR-1 and Ag3PO4. Environ. Int. 126, 560–567. https://doi.org/10.1016/j.envint.2019.03.010.

Yu, X., Zhao, Z., Zhang, J., Guo, W., Li, L., Liu, H., Wang, Z.L., 2017. One-step synthesis of ultrathin nanobelts-assembled urchin-like anatase TiO_2 nanostructures for highly efficient photocatalysis. CrysEngCommun 19, 129–136. https://doi.org/10.1039/c6ce02241c.

Yusuf, T.L., Orimolade, B.O., Masekela, D., Mamba, B., Mabuba, N., 2022. The application of photoelectrocatalysis in the degradation of rhodamine B in aqueous solutions: a review. RSC Adv. 12, 26176–26191. https://doi.org/10.1039/D2RA04236C.

Zhang, J., Vasei, M., Sang, Y., Liu, H., Claverie, J.P., 2016. TiO_2@carbon photocatalysts: the effect of carbon thickness on catalysis. ACS Appl. Mater. Interf. 8, 1903–1912. https://doi.org/10.1021/acsami.5b10025.

Zhang, Y., Zhou, J., Cai, W., Zhou, J., Li, Z., 2018. Enhanced photocatalytic performance and degradation pathway of rhodamine B over Hierarchical Double-Shelled Zinc Nickel oxide Hollow Sphere heterojunction. Appl. Surf. Sci. 430, 549–560. https://doi.org/10.1016/j.apsusc.2017.06.325.

Zhao, Z., Liu, J., Sa, G., Xu, A., 2022. Electronic properties and photodegradation ability of Nd-TiO_2 for phenol. J. Rare Earths 40, 1063–1072. https://doi.org/10.1016/j.re.2021.08.007.